Title: Mixed Alcohol Dehydration over Brønsted and Lewis Acidic Catalysts

Authors: Connor P. Nash[a], Anand Ramanathan[b], Daniel A. Ruddy[c], Mayank Behl[a], Erica Gjersing[a], Michael Griffin[a], Hongda Zhu[b], Bala Subramaniam[b], Joshua A. Schaidle[a], and Jesse E. Hensley*[,a]

[a]National Bioenergy Center, National Renewable Energy Laboratory, Golden, CO 80401, USA
[b]Center for Environmentally Beneficial Catalysis, The University of Kansas, Lawrence, KS 66047, USA
[c]Chemistry and Nanoscience Center, National Renewable Energy Laboratory, Golden, CO 80401, USA

*Corresponding Author Information: 15013 Denver West Parkway, Golden, Colorado 80401, USA
Email: Jesse.Hensley@NREL.gov

Abstract

Mixed alcohols are attractive oxygenated products of biomass-derived syngas because they may be catalytically converted to a range of hydrocarbon products, including liquid hydrocarbon fuels. Catalytic dehydration to form olefins is a potential first step in the conversion of C_2-C_4 alcohols into longer-chain hydrocarbons. We describe here the physical and chemical characterization along with catalytic activity and selectivity of four Brønsted and Lewis acidic catalysts for the dehydration of two mixed alcohol feed streams that are representative of products from syngas conversion over K-CoMoS type catalysts (i.e., ethanol, 1-propanol, 1-butanol and 2-methyl-1-propanol). Specifically, a Lewis acidic Zr-incorporated mesoporous silicate (Zr-KIT-6), a commercial Al-containing mesoporous silicate (Al-MCM-41), a commercial microporous aluminosilicate (HZSM-5), and a commercial microporous silicoaluminophosphate (SAPO-34) were tested for mixed alcohol dehydration at 250, 300 and 350 °C. The zeolite materials exhibited high activity (>98% ethanol conversion) at all temperatures while the mesoporous materials only displayed significant activity (>10% ethanol conversion) at or above 300 °C. The turnover frequencies for ethanol dehydration at 300 °C decreased in the following order: HZSM-5 > SAPO-34 > Al-MCM-41 > Zr-KIT-6, suggesting that Brønsted acidic sites are more active than Lewis acidic sites for alcohol dehydration. At 300 °C, SAPO-34 produced the highest yield of olefin products from both a water-free ethanol rich feed stream and a C_{3+}-alcohol rich feed stream containing water. Post-reaction characterization indicated changes in the Brønsted-to-Lewis acidic site ratios for Zr-KIT-6, Al-MCM-41 and HZSM-5. Ammonia temperature programmed desorption indicated that the acid sites of post-reaction samples could be regenerated following treatment in air. The post-reaction SAPO-34 catalyst contained more aromatic, methylated aromatic and polyaromatic compounds than its zeolite counterpart HZSM-5, while no aromatic compounds were observed on post-reaction Al-MCM-41 or Zr-KIT-6 catalysts. Olefin yield at 300 °C over SAPO-34 (>95%) was comparable to published values for the methanol-to-olefins process, indicating the potential industrial application of mixed alcohol dehydration. Furthermore, the olefin product distribution over SAPO-34 was tunable by the composition of the alcohol feed mixture.

Graphical Abstract

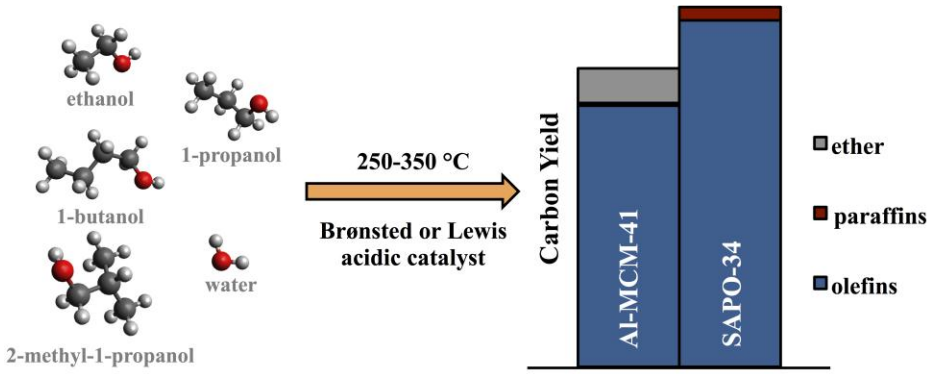

Keywords: mixed alcohols, dehydration, olefin, SAPO-34, syngas

1. Introduction

In recent years, significant effort has been placed on the cost competitive production of transportation fuels from non-food biomass [1-5]. The gasification of lignocellulosic biomass to produce syngas followed by additional chemical transformations is one approach for producing hydrocarbons for chemical and fuel use [6,7]. This process has also been referred to as indirect liquefaction [8]. A variety of products can be produced from syngas, including hydrogen, alkanes, methanol, and mixed alcohols [9]. The methanol-to-olefin (MTO) process is an industrial example of olefin production from syngas-derived methanol, but suffers from limitations in the ethylene to propylene product ratio [10]. The MTO process is typically operated between 450-525 °C and 34-345 kPa [11]. The ability to target precise ratios of a more diverse olefin product would be advantageous for the downstream production of hydrocarbons with a greater carbon number distribution via oligomerization.

Previous research from the National Renewable Energy Laboratory has demonstrated the ability to convert biomass-derived syngas to a mixed alcohol product containing primarily ethanol, with lesser amounts of methanol, 1-propanol, isobutanol, 1-butanol, methyl formate, ethyl formate, ethyl acetate, acetaldehyde, and propionaldehyde [7]. Transforming a mixed alcohol product into liquid fuel-range hydrocarbons using a moderate-temperature, low-pressure process remains a challenge. Catalytic dehydration is a potential first step in the conversion of C_2-C_4 alcohols into longer-chain hydrocarbons. Following dehydration, the resulting olefins can be oligomerized to produce naphtha and distillate fuels, providing an option for producing hydrocarbons from syngas.

SAPO-34 is the preferred catalyst for converting methanol to ethylene and propylene [10,12,13], and has demonstrated high activity for ethanol, 1-butanol and 2-butanol dehydration [14,15]. Other solid acid zeolite catalysts such as HZSM-5 have also been studied extensively for alcohol dehydration reactions [16-21]. In addition to zeolite materials, metal-containing mesoporous silica-based materials (e.g., Ni-MCM-41 and Zr-KIT-6) are capable of dehydrating a variety of alcohols to the corresponding olefin products [22-26]. The nature of the acid sites (type and strength) has also been shown to effect alcohol dehydration performance. Strong Brønsted acidic zeolites often suffer from poor selectivity to desired products [16,27,28] and are prone to coke deposition and short operable lifetimes [27,29,30]. There is evidence that materials with lower Brønsted to Lewis acid ratios exhibit higher selectivity and stability in alcohol dehydration reactions [23,31]. Despite the extensive analyses of alcohol dehydration to olefins, a performance comparison of zeolite and mesoporous silica catalysts for dehydration of *mixed alcohols* has not been reported.

Here we report a comparison of the performance of a Lewis acidic Zr-incorporated mesoporous silicate [Zr-KIT-6 (Si/Zr = 20)], a commercial Al-incorporated mesoporous silicate [Al-MCM-41 (Si/Al = 78)], and two commercial zeolites (HZSM-5 and SAPO-34) for dehydration of mixed alcohols. Two mixed alcohol feeds, representative of products of mixed alcohol synthesis from syngas over K-CoMoS type catalysts [7], were tested between 250 and 350 °C. The mixed alcohol feeds were composed of varying concentrations of ethanol, 1-propanol, 1-butanol, 2-methyl-1-propanol and water. Product selectivity and olefin yields achieved from mixed alcohol dehydration are compared to those from the MTO process. Catalyst samples were analyzed before and after reaction for evidence of coking, acid site modifications and crystalline structural changes. The results suggest that olefin yields comparable to the MTO process are achievable at lower temperature, and that the olefin composition is tunable by the alcohol feed composition.

2. Experimental Section

2.1. Catalyst Characterization

2.1.1. BET Surface Area. Nitrogen physisorption data were collected at -196 °C using a Quantachrome Quadrasorb SI instrument. Samples were pre-treated under vacuum for 20 h at 200 °C. Surface areas were determined using the Brunauer-Emmett-Teller (BET) method, and pore volumes were determined from the adsorption isotherm data using the Barrett-Joyner-Halenda (BJH) method. For zeolite materials (SAPO-34 and HZSM-5), the P/P_0 range of 0.01 – 0.08 was used to determine the BET surface area. For mesoporous silica-based materials (Al-MCM-41 and Zr-KIT-6), the P/P_0 range of 0.05 – 0.30 was used to determine the BET surface area. Pore diameters for Zr-KIT-6 and Al-MCM-41 were determined from the adsorption

isotherm using the BJH method, by taking the maximum point on the plot of dV(log d) versus pore diameter (d). For zeolite materials, the micropore sizes are reported based on the crystalline parent structures of MFI (HZSM-5) and CHA (SAPO-34) zeolites according to the International Zeolite Association *Database of Zeolite Structures* [32].

2.1.2. X-ray Diffraction. Powder X-ray diffraction (PXRD) data were collected using a Rigaku Ultima IV diffractometer with a Cu Kα source using a D/teX Ultra high-speed detector. Diffractograms were collected in the 2θ range of 5 – 80 degrees at a scan rate of 5 °/min. Samples were prepared by supporting the powdered catalyst onto a glass slide having a 0.5 mm recession and pressing with a glass slide to create a uniform z-height. Small Angle X-ray Scattering (SAXS) diffractograms were collected in the 2θ range of 0.5-4.0 degrees at a scan rate of 0.05 °/min and a scan width of 0.005 degrees using a scintillation counter. The diffractometer was operated at 40 kV and 44 mA for PXRD and SAXS measurements.

2.1.3. Total Acid Site Titration: NH_3-TPD. The total number of acid sites was determined by NH_3 temperature programmed desorption (NH_3-TPD) using an Altamira Instruments AMI-390 system with gas flow rates of 25 mL/min. Catalyst samples (ca. 200 mg) were loaded into a quartz U-tube reactor and held as a fixed bed between plugs of quartz wool. All catalyst samples were first heated to 500 °C at 2 °C/min in 10% O_2/Ar and held for 5 h. Following pretreatment, samples were cooled to 120 °C in flowing He and then saturated with flowing 10% NH_3/He for 3 h. Excess and/or physisorbed NH_3 was removed by holding the samples at 120 °C in flowing He for 0.5 h. NH_3-TPD was performed by heating the sample from 120 °C to 500 °C at 30 °C/min, and then holding at 500 °C for 0.5 h in flowing He. Desorbed NH_3 was measured with a thermal conductivity detector, and calibration was performed after each experiment by introducing 10 pulses of 10% NH_3/He from a 5 mL sample loop into a stream of flowing He. The quantification of surface sites was done assuming adsorption stoichiometry of one NH_3 molecule per acid site [33,34].

2.1.4. Brønsted and Lewis Acid Site Titration: Pyridine DRIFTS. The relative amounts of Lewis and Brønsted acidic sites were determined using pyridine adsorption diffuse-reflectance FT-IR spectroscopy (py-DRIFTS), which was recorded on a Thermo Nicolet iS50 FT-IR spectrometer operating at 4 cm^{-1} resolution equipped with a Harrick praying mantis reaction chamber and Si windows. For analysis of fresh catalysts, samples were loaded into the chamber and pretreated in flowing air at 2 °C/min to 500 °C for zeolites and 10 °C/min to 500 °C for silica materials, and held at this temperature for 3 h. Post-reaction samples were pre-treated in flowing nitrogen at their reaction temperature (250, 300, or 350 °C), and held at this temperature for 0.5 h. After cooling to 150 °C, the sample was purged with nitrogen for 0.5 h, and pyridine vapor was introduced. After 3 min of pyridine exposure, the sample was heated to 300 °C at 10 °C/min and held for 0.5 h under flowing nitrogen to remove excess and/or physisorbed pyridine. The pressure throughout the pre-treatment, dosing, and desorption procedures was atmospheric. The absorption bands near 1445 cm^{-1} (Lewis) and 1545 cm^{-1} (Brønsted) and their relative absorption coefficients ($\varepsilon_B/\varepsilon_L$ = 0.76) were used to determine the relative Brønsted/Lewis acidic site ratios [35,36].

2.1.5. Post-Reaction Organic Species: Solution ^1H NMR. The amount of soluble organic material remaining on the catalyst surface after reaction was determined using ^{1}H NMR spectroscopy. Solution-phase ^{1}H NMR spectra were recorded using a Varian Inova 400 MHz spectrometer. Spectra were collected for 16 scans with a pulse width of 4.8 μsec, a recycle delay of 1 s. Post-reaction catalyst samples (ca. 100 mg) were combined with solvent (1.0 mL of $CDCl_3$) and an internal standard (5.0 μL CH_2Br_2) in a sealed sample vial. The vial was sonicated briefly before being filtered directly into an NMR tube and analyzed for solubilized organics.

2.1.6. Post-Reaction Organic Species: Solid-State NMR. Organic species remaining on the catalyst surface after reaction were determined by solid-state NMR. Solid-state NMR spectra of catalyst samples were acquired with a 200 MHz Bruker Avance III spectrometer equipped with a 4.7 T magnet. Resonant frequencies were ^{1}H=200.1 MHz and ^{13}C=50.3 MHz and a cross polarization magic angle spinning (CPMAS) spectra was acquired with a 7.0 mm CPMAS probe and ZrO_2 rotors. A ramped CP pulse with ^{1}H and ^{13}C fields matched at 48.0 kHz was applied with a contact pulse of 2.0 ms. Each spectra was collected for 10 k or 30 k scans, in order to obtain spectra with a sufficient signal to noise ratio, with MAS=5.0 kHz and a recycle delay of 2.0 s. Spectra were integrated to provide a relative distribution of post-reaction species.

2.1.7. Elemental Analysis. Elemental analysis of post-reaction catalyst samples was performed by Galbraith Laboratories, Inc. (Knoxville, TN) to determine the carbon and hydrogen content. A fresh Al-MCM-41 catalyst sample was also analyzed by inductively coupled plasma atomic emission spectroscopy to determine if any impurities (e.g., Fe) were present.

2.2. Mixed Alcohol Dehydration

2.2.1. Materials. HZSM-5 (Si/Al = 15 mol/mol) was obtained from Nexceris. Al-MCM-41 (Si/Al = 78 mol/mol) and SAPO-34 (Si/Al = 0.20 mol/mol) were purchased from ACS Materials. Zr-KIT-6 (Si/Zr = 20 mol/mol), a Lewis acidic large pore-cubic *Ia3d* mesoporous silicate, was synthesized as previously reported [25]. All catalysts were pressed, crushed and sieved to an agglomerate size of 300-500 µm. For each experiment, ca. 750 mg of catalyst was physically mixed with an appropriate amount of an inert, low surface-area diluent, silicon carbide (SiC), to a volume equal to the isothermal zone of the reactor (3 mL). The mass of SiC used ranged between 1.1 and 4.7 g due to differences in the bulk densities of the various catalysts. The diluent was used to prevent channeling, to mitigate axial dispersion problems, and to minimize temperature gradients in the catalyst bed.

2.2.2. Catalytic Testing: Mixed Alcohol Dehydration. Mixed alcohol dehydration experiments were performed at 250, 300 and 350 °C in a downward-flow stainless steel tubular packed bed reactor (ID = 7.1 mm). The diluted catalyst was positioned in the isothermal zone of the reactor between quartz wool and quartz chips. A four-point thermocouple centered in the catalyst bed was used to monitor reaction temperature, which was maintained at +/- 0.5 °C. Feed and effluent tubing was heated to prevent condensation of vapors.

Prior to reaction, all catalysts were activated in flowing air with heating to 500 °C at 2 °C/min. Catalysts were held at 500 °C for at least 4 h before being brought to reaction temperature in flowing argon. Table 1 provides the molar composition of the two mixed alcohol feed mixtures studied. Mixed alcohol streams were selected by estimating probable outputs from a commercial crude mixed alcohol reactor coupled with separation and recycle operations [7,8]. An additional assumption was made that trace sulfides, aldehydes, esters, and water, expected to exist in the mixed alcohol product, are removed, for purposes of elucidating the impacts of mixtures of alcohols on conversion absent of competing reactions with other oxygenates (denoted as ethanol rich mixture). An additional scenario, assuming incomplete removal of water and partial recycle of ethanol to the mixed alcohol reactor to net higher yields of C_{3+}-alcohols, was used as a second surrogate feed (denoted as C_{3+}-alcohol rich mixture). Liquid reactants were fed to the reactor using a Waters nanoAcquity pump. Nitrogen and argon were used as the carrier gas and internal standard, respectively. Experiments were run at three weight-hourly space velocities (WHSV). Each WHSV was held for 2.5-3.0 h while gas samples were collected. Here, WHSV was defined as the total mass flow rate of alcohol reactants in the feed divided by the catalyst mass. Before collecting gas samples, the system was allowed to equilibrate for 20 min. At each WHSV condition, one inlet and two outlet gas samples were analyzed via a gas chromatogram (GC). An additional outlet gas sample was taken for each WHSV and analyzed with a mass spectrometer detector (MSD) to identify product species. The flow rates of the nitrogen, argon and the alcohol feed stream were adjusted to vary the WHSV while keeping the mole fraction (and hence partial pressure or activity) of the alcohol stream constant (2.3-2.5 mol%). The reactor pressure relative to atmospheric pressure varied slightly as a function of WHSV, ranging from 21-83 kPa.

Table 1. Alcohol feed mixtures for mixed alcohol dehydration experiments.

Component	Mole %	
	Ethanol Rich	**C_{3+}-Alcohol Rich**
Ethanol	98.8	64.4
1-Propanol	1.17	27.0
1-Butanol	0.0148	5.31
2-Methyl-1-Propanol	0.0123	2.57
Water	-	0.720

2.2.3. Product Analysis. An online GC/MS (Agilent GC 7980A/5977 MSD) was used to sample hot inlet feeds and outlet product gases for quantitative analysis. The GC/MS was equipped with a flame ionization detector for quantification of hydrocarbons and oxygenates, a thermal conductivity detector for quantification of permanent gases and water and a MSD for compound identification. The GC/MS was calibrated using gas and liquid standards containing reactant and product compounds of known concentration. Gas standards were purchased from Air Liquide and liquid standards were prepared gravimetrically. For most experiments, mass balances closed to 100 +/-10%. The alcohol conversion, X_i, was calculated according to equation (1):

$$X_i = \frac{\dot{n}_{in,i} - \dot{n}_{out,i}}{\dot{n}_{in,i}} * 100\% \quad (1)$$

where $\dot{n}_{in,i}$ and $\dot{n}_{out,i}$ represent inlet and outlet molar flow rates for alcohol i, respectively. Inlet molar flow rates were calculated according to equation (2):

$$\dot{n}_{in,i} = \frac{\dot{m}_{in,tot} * x_{in,i}}{FW_{in}} \quad (2)$$

where $\dot{m}_{in,tot}$ is the total mass flow rate at the reactor inlet, $x_{in,i}$ is the mole fraction of alcohol i and FW_{in} is the formula weight of the inlet stream. Outlet molar flow rates were calculated according to equation (3):

$$\dot{n}_{out,i} = \frac{\dot{n}_{out,Ar} * x_{out,i}}{x_{out,Ar}} \quad (3)$$

where $x_{out,i}$ and $x_{out,Ar}$ are the mole fractions of alcohol i and argon in the outlet. Argon was used as an internal standard such that the outlet molar flow rate, $\dot{n}_{out,Ar}$, was assumed to equal the inlet molar flow rate as defined by equation (4):

$$\dot{n}_{out,Ar} \equiv \dot{n}_{in,Ar} \quad (4)$$

Conversions were only calculated for ethanol and 1-propanol in the ethanol rich feed experiments because 1-butanol and 2-methyl-1-propanol concentrations were below the detection limit of the GC. Similarly, 2-methyl-1-propanol was below the detection limit of the GC in the C_{3+}-alcohol rich experiments. Carbon selectively to products, S_i, was calculated via equation (5):

$$S_i = \frac{c_i n_i}{\sum c_i n_i} * 100 \quad (5)$$

where c_i and n_i represent concentration and carbon number, respectively, for individual oxygenate and hydrocarbon products. The product carbon yield, Y_i, for each species was calculated according to equation (6):

$$Y_i = X_T * S_i * 100 \quad (6)$$

where X_T is the total carbon conversion defined by equation (7):

$$X_T = \frac{\dot{n}_{c,in} - \dot{n}_{c,out}}{\dot{n}_{c,in}} \quad (7)$$

where $\dot{n}_{c,in}$ and $\dot{n}_{c,out}$ represent inlet and outlet molar flow rates of carbon in reactant species.

2.2.4. Catalytic Testing: Ethanol Dehydration Kinetics. Intrinsic kinetic studies were performed with a fixed bed reactor and the temperature was controlled and monitored to achieve a steady-state temperature of 300.0 ± 0.2 °C. The reactor effluent line was connected to a HP 5890 GC equipped with a ZB-WAX column configured for online analysis. In order to obtain finite conversions even at high space velocities, the SAPO-34 and HZSM-5 samples were diluted with inert silica sand (Sigma-Aldrich) in a ratio of 20:1 by weight, silica to catalyst. The catalyst samples were pretreated for 5 h at 500 °C in flowing air (from Zero Air Generator, Matheson). Ethanol (absolute, > 99.5%, Acros) was pumped with an ISCO syringe pump, then vaporized in a heated line and mixed with flowing nitrogen (Matheson). The mixed gas stream was then passed through the fixed bed, and directed to the GC for analysis. Catalyst loading and total mass flow rates were varied to adjust WHSV and ethanol conversion. The ethanol concentration was maintained at 1.5 mol%. The turnover frequency (TOF) based on steady-state ethanol conversion was calculated according to equation (5):

$$TOF_{ethanol} = \frac{\frac{WHSV}{MW_{ethanol}} * X_{ethanol}}{A_{NH_3}} \quad (5)$$

where *WHSV* is the weight-hourly space velocity of ethanol, $MW_{ethanol}$ is the molecular weight of ethanol, $X_{ethanol}$ is the steady-state ethanol conversion and A_{NH3} is the acid site density in μmol/g of the fresh catalyst as determined by NH_3-TPD. Equation (6) was used to calculate TOFs based on ethylene or diethyl ether production:

$$TOF_i = \frac{\frac{WHSV}{MW_{ethanol}} * X_{ethanol} * S_i}{A_{NH_3}} \quad (6)$$

where S_i is the fractional carbon selectivity and *i* is either ethylene or diethyl ether.

3. Results and Discussion

3.1. Structural and Chemical Catalyst Characterization: Pre Reaction

The SAPO-34 and HZSM-5 zeolite materials exhibited surface areas in the typical range of 400–600 m^2/g, with characteristic pore volumes (Table 2). For the Al-MCM-41 and Zr-KIT-6 materials, the characteristic type IV isotherms were observed, indicative of mesoporosity and accompanied by a narrow pore size distribution (Supporting Information Figure S1). As expected, the mesoporous Al-MCM-41 and Zr-KIT-6 exhibited greater surface areas and pore volumes than the zeolite materials.

Table 2. Surface area (S_{BET}), pore volume (V_p), and average pore diameter (d_p) of catalysts determined by N_2 physisorption.

Catalyst	S_{BET} (m^2/g)	V_p (cm^3/g)	d_p (nm)
Zr-KIT-6	770	1.4	9.8
Al-MCM-41	1020	1.3	3.5
SAPO-34	590	0.014	0.50[a]
HZSM-5	430	0.20	0.63[a]

[a]Pore size according to crystallographic data [32]

SAXS and PXRD patterns for the pre-reaction catalyst samples are shown in Figures 1 and 2, respectively. SAXS patterns were collected to probe nano-scale features (i.e., ordered mesopores) that are observed at lower 2θ values compared to peaks at larger 2θ values, which correspond to crystal lattice spacing. The SAXS pattern of the Zr-KIT-6 catalyst displayed an intense peak at 2θ= 0.9 ° with a subtle shoulder at 2θ= 1.0 ° (Figure 1a). These two peaks are indicative of the (211) and (220) reflections, confirming a well-ordered mesoporous structure with cubic *Ia3d* symmetry [25,37,38]. The broad peak observed in the range of 20-30 ° in the XRD pattern for Zr-KIT-6 corresponds to amorphous silica; however, there were no reflections corresponding to crystalline ZrO_2 or $ZrSiO_4$ phases, which suggests that the Zr species are well-dispersed in the amorphous silica matrix [37]. These results corroborate previously reported data on Zr-KIT-6 [25,37]. The XRD pattern for Al-MCM-41 also displays a broad peak between 20-30 ° without any crystalline alumina phases, as expected for amorphous Al-MCM-41 (Figure 2b). The SAXS pattern displays a broad peak at 2.0 ° similar to patterns for metal-incorporated MCM-41 found in the literature, indicating some degree of mesoporosity [38]. The zeolites, SAPO-34 and HZSM-5, do not have mesoporous-type features and thus did not display any major peaks in their SAXS patterns (Figure 1c and 1d). The XRD patterns for SAPO-34 and HZSM-5 matched their JCPDS reference files (00-055-0829 and 00-037-0359, respectively). Peaks in the small angle diffractograms at 2θ values of 1.4 ° and 2.3 ° (or 1.1 ° and 1.7 ° due to minor adjustments to the Rigaku instrument) are background peaks from the glass tray used to support these materials during X-ray experiments (Figure S2).

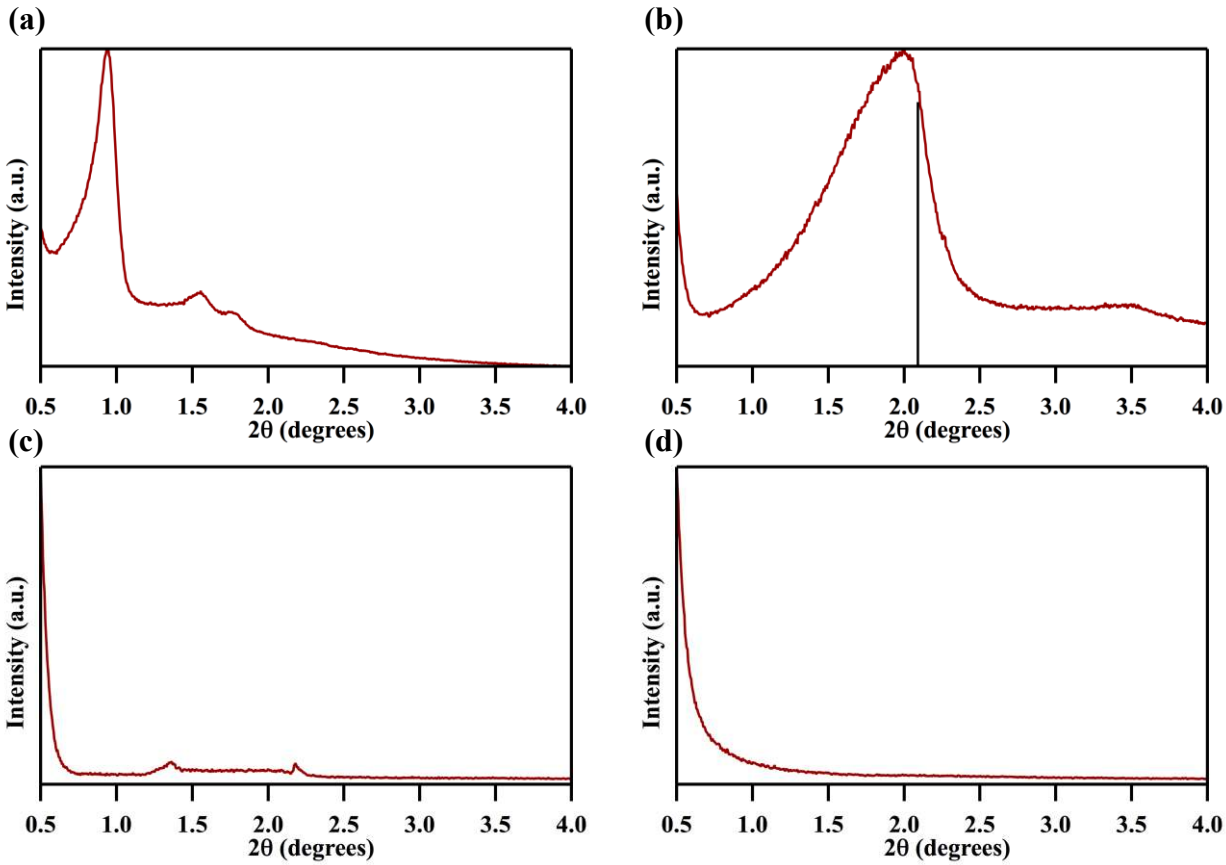

Figure 1. Small angle scattering patterns for fresh (a) Zr-KIT-6, (b) Al-MCM-41, (c) SAPO-34 and (d) HZSM-5 catalysts. Reference diffraction patterns are shown where available (black lines). Peaks in (c) at 2θ= 1.4 ° and 2.25 ° are due to the glass support slide.

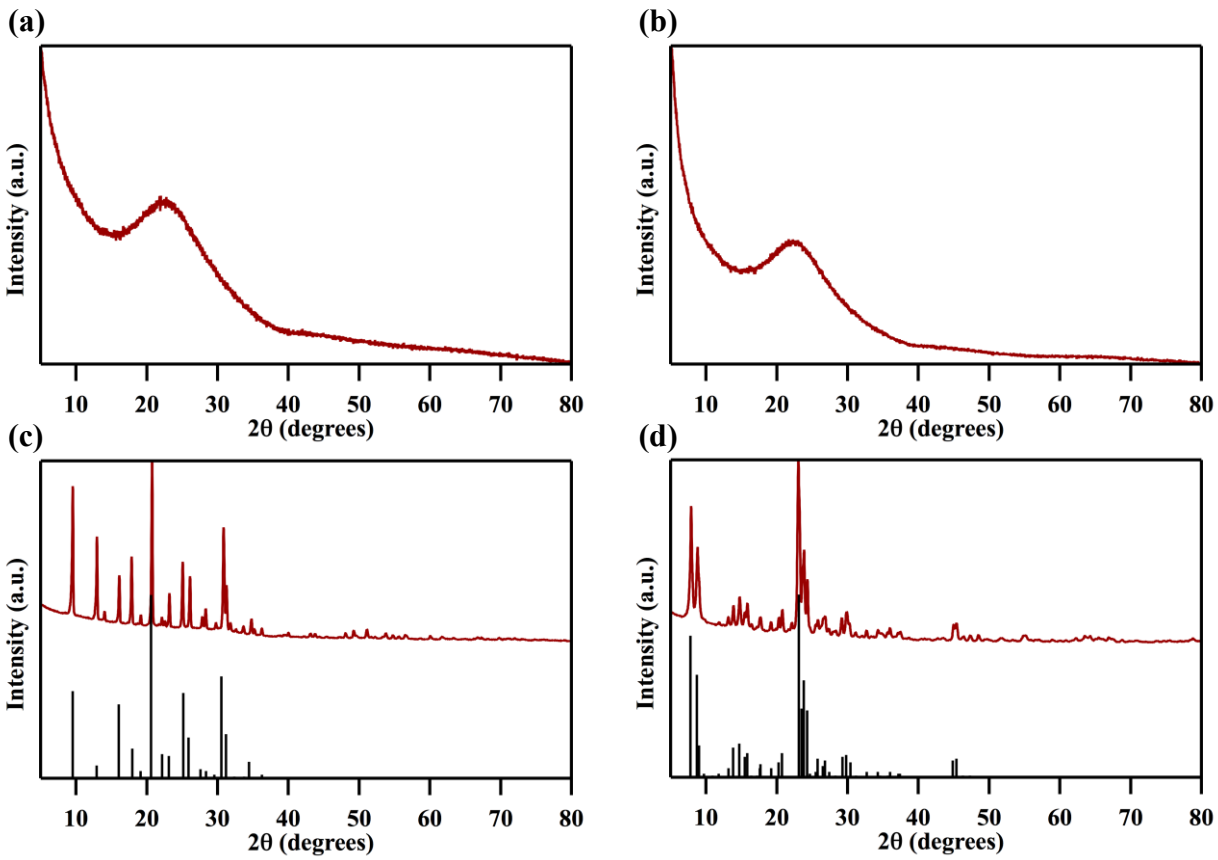

Figure 2. Powder X-Ray diffractograms for fresh (a) Zr-KIT-6, (b) Al-MCM-41, (c) SAPO-34, and (d) HZSM-5 catalysts. Reference diffraction patterns are shown where available (black lines).

3.2. Acid Site Characterization: Pre-Reaction

The measured values for total, Brønsted, and Lewis acidic sites are presented in Table 3. The SAPO-34 catalyst could not be analyzed using py-DRIFTS since the pyridine probe molecule is too large to fit into 0.5 nm pores [39]. The NH_3-TPD profiles for HZSM-5 and SAPO-34 resembled literature reports, exhibiting two peaks in the range of 200–500 °C (Figure S3) [40,41]. The total acid site value for HZSM-5 was similar to the theoretical value of 1050 µmol/g for this material. In contrast, the total acid site density for SAPO-34 was greater than the theoretical value of 1480 µmol/g. However, the calculated value does not take into account any Brønsted sites generated from surface P-OH groups. The measured value of 1700 µmol/g corresponds to 12% of the P atoms providing an acidic P-OH. The fresh Al-MCM-41 contained 0.55 wt% Al, 0.2 wt% Ca, and 0.08 wt% Fe as determined by ICP, with a Si/Al ratio of 78. The Al-MCM-41 material exhibited a weak TPD signal, and a low overall acidity of 264 µmol/g. The aluminum incorporation is primarily responsible for the enhanced acidity of Al-MCM-41. The incorporation of Zr into a silica framework of KIT-6 results in an acidic material that exhibited one broad peak in the TPD profile corresponding to 785 µmol/g. The Brønsted versus Lewis nature of the acid sites differs greatly between the HZSM-5 zeolite and the mesoporous materials (py-DRIFTS plots shown in Figure S4). HZSM-5 is predominantly Brønsted-acidic, having a B/L molar ratio of 13.25. In contrast, the mesoporous catalysts are predominantly Lewis-acidic, having low B/L molar ratios of 0.03 and 0.11. In addition, the higher-temperature NH_3 desorption peak of HZSM-5 compared to Zr-KIT-6 is indicative of stronger acid sites (Figure S3).

Table 3. Acid site characterization on fresh, activated catalysts from NH_3-TPD and py-DRIFTS.

Catalyst	Total Acid Sites (µmol/g)	B/L ratio	Brønsted Sites (µmol/g)	Lewis Sites (µmol/g)
Zr-KIT-6	785	0.11	78	707
Al-MCM-41	264	0.03	8	256
SAPO-34	1700	n/a[a]	-	-
HZSM-5	998	13.25	928	70

[a]py-DRIFTS data for SAPO-34 unavailable because the pyridine probe molecule is too large to fit into 0.5 nm pores [39]

3.3. Mixed Alcohol Dehydration

3.3.1. Ethanol Conversion. The ethanol conversion as a function of WHSV and time-on-stream (TOS) for each experiment is plotted in Figure 3. At 250 °C, the Al-MCM-41 and Zr-KIT-6 catalysts displayed low activity (<10% ethanol conversion). The ethanol conversion for both catalysts was dramatically higher at and above 300 °C, and increased as the space velocity was decreased. Both HZSM-5 and SAPO-34 displayed high activity in all experiments (ethanol conversion >98%). HZSM-5 and Zr-KIT-6 have comparable numbers of total acidic sites (Table 3), but HZSM-5 was significantly more active than the Lewis acidic sites of Zr-KIT-6.

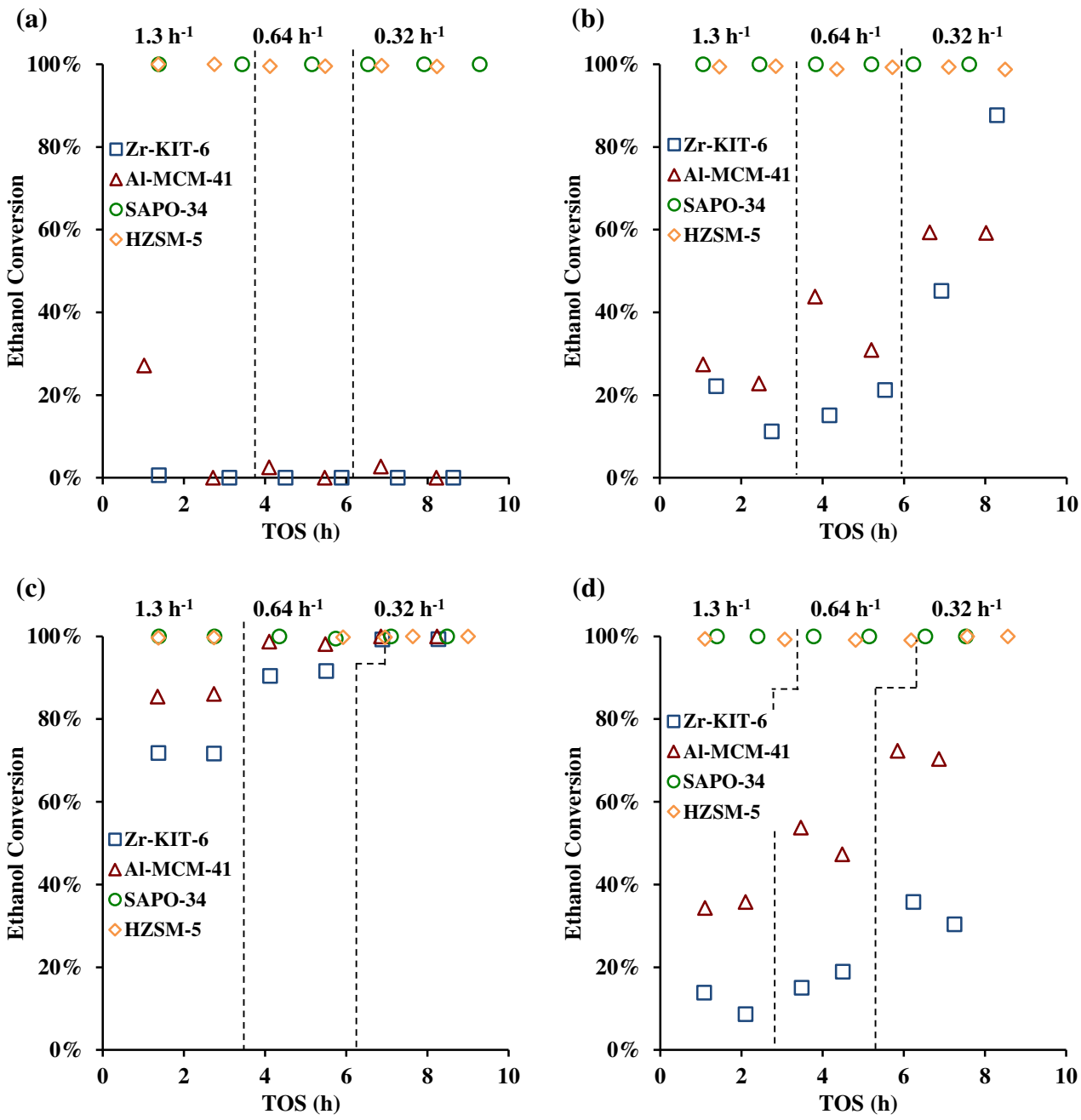

Figure 3. Ethanol conversion in mixed alcohol dehydration experiments as a function of time-on-stream and WHSV for experiments with the ethanol rich alcohol feed at (a) 250 °C, (b) 300 °C, (c) 350 °C, and (d) with the C_{3+}-alcohol rich feed at 300 °C for each catalyst.

3.3.2. Product Yield. The carbon yield to unbranched olefins (e.g., ethylene, propylene, *trans*-2-butene), branched olefins (e.g., isobutylene, 2,3-methyl-1-butene), unbranched paraffins (e.g., ethane, propane, butane), branched paraffins (e.g., isobutane, 2-methylbutane, 2,3-dimethylbutane) and diethyl ether at 300 °C and WHSV 0.32 h^{-1} are presented in Figure 4a and 4c for the ethanol rich and C_{3+}-alcohol rich feeds, respectively. Products with five or more carbons were grouped together as C_{5+} and other byproducts (e.g.,

methanol, propanal, carbon monoxide and carbon dioxide) were included as 'other'. Similar groupings were made in Figure 5 for data at 250 and 350 °C. Total product yield at 300 °C was highest for the zeolite catalysts (>98%) and lowest for the mesoporous silica-based catalysts (<65%, Figure 4a). Due to low ethanol conversion, the total carbon yield over the mesoporous materials at 250 °C was less than 10% (Figure 5a-b); however, all catalysts displayed total product yields greater than 98% at 350 °C (Figure 5c-d). Total product yield was maintained at >98% at all temperatures over HZSM-5 and SAPO-34. Table 4 presents the TOF for each catalyst from ethanol dehydration kinetics experiments. Based on TOFs for ethanol conversion, the intrinsic dehydration activity of the catalyst acidic sites followed the order: HZSM-5 > SAPO-34 > Al-MCM-41 > Zr-KIT-6. Due to the high activity of HZSM-5, the lowest achievable conversion in the ethanol dehydration kinetic experiments was 34% and thus the TOF presented for HZSM-5 may be an under-prediction of the intrinsic ethanol dehydration activity (Figure S5). Differences in product selectivity were also observed in kinetic experiments with ethanol. Of particular interest is the significant selectivity to diethyl ether observed over SAPO-34 (Table 4 and Figure S5). No diethyl ether was observed over SAPO-34 in mixed alcohol dehydration experiments (Figures 4 and 5), though the level of ethanol conversion was significantly higher.

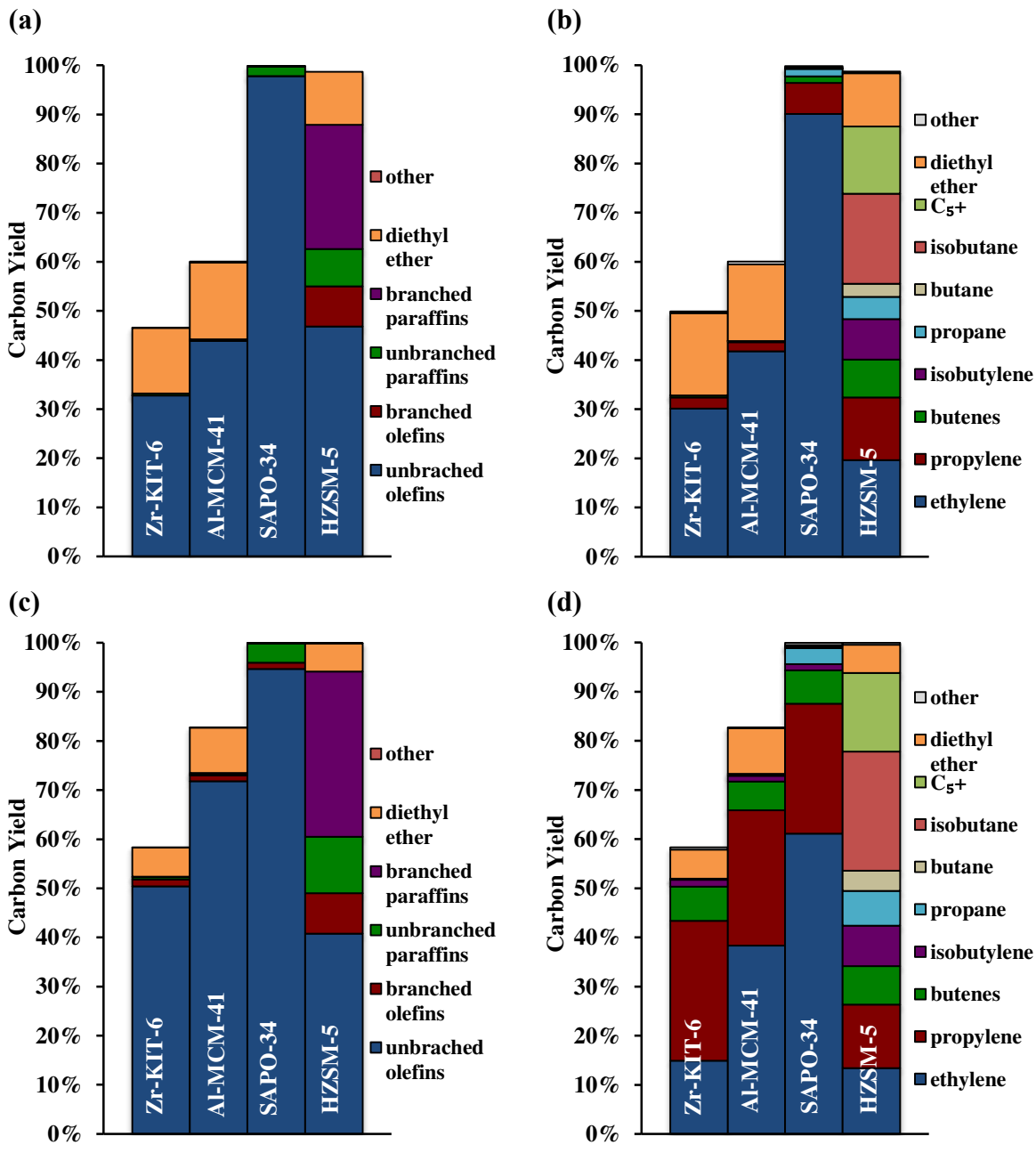

Figure 4. Carbon yield for mixed alcohol dehydration experiments at 300 °C and WHSV = 0.32 $h^{-1}$from the (a-b) ethanol rich mixed alcohol feed and (c-d) C_{3+}-alcohol rich feed. Data is grouped by (a, c) functional group and branching and by (b, d) major product species. 'Other' corresponds to the sum of carbon monoxide, carbon dioxide, propanal and methanol. Data is presented as average of replicate data points at WHSV = 0.32 h^{-1} except for Zr-KIT-6 in (a-b) which is presented as the first data point at WHSV = 0.32 h^{-1}.

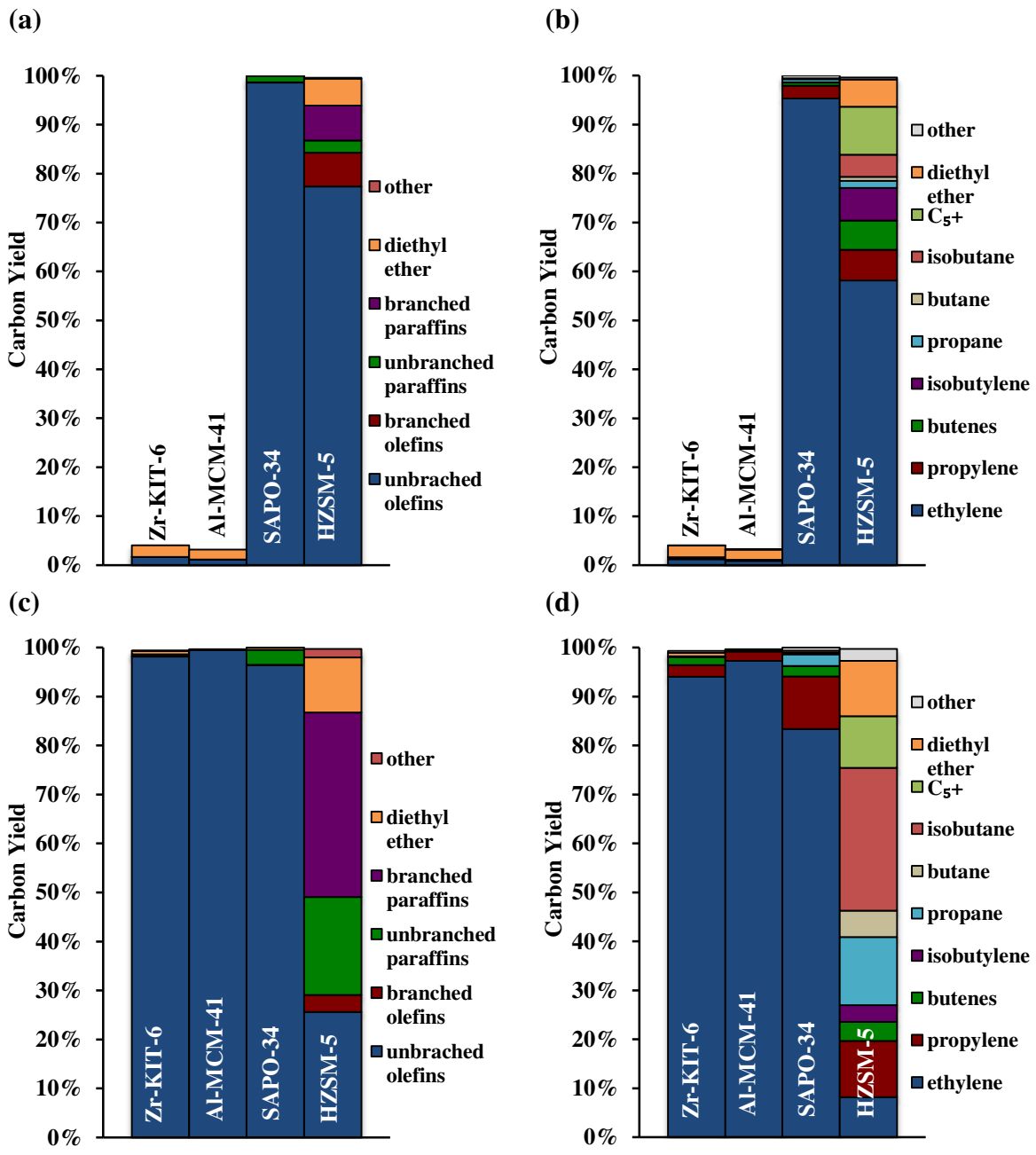

Figure 5. Carbon yield from mixed alcohol dehydration experiments with the ethanol rich mixed alcohol feed at (a-b) 250 °C and (c-d) 350 °C. Data is grouped by (a, c) functional group and branching and by (b, d) major product species. 'Other' products are carbon monoxide, carbon dioxide, propanal and methanol. Data is presented as average of replicate data points at WHSV = 0.32 h^{-1}.

Table 4. Intrinsic ethanol dehydration kinetic parameters at 300 °C.

	TOF (s^{-1}): Ethanol Conversion	TOF (s^{-1}): Ethylene Production	TOF (s^{-1}): Diethyl Ether Production	Ethanol Conversion (%)
Zr-KIT-6	0.0019	0.0015	0.00039	6.9
Al-MCM-41	0.0064	0.0035	0.0035	6.9
SAPO-34	0.028	0.019	0.0087	7.4
HZSM-5*	0.73	0.60	0.13	34

*Lowest achievable ethanol conversion was 34%

The two mesoporous silica-based materials, Zr-KIT-6 and Al-MCM-41, exhibit similar product selectivities in ethanol-rich feed experiments at 300 °C despite different total product carbon yields, and both catalysts form diethyl ether in non-negligible quantities (Figure 4a). Selectivity to unbranched olefins increased with temperature over the mesoporous catalysts. In ethanol-rich feed experiments at 300 °C, SAPO-34 also displayed high selectivity to unbranched olefins (Figure 4a) while HZSM-5 displayed higher selectivity to paraffin products. The yield of unbranched olefins was only 46% over HZSM-5 at 300 °C, whereas the yield of branched and unbranched paraffins was 25% and 7.5%, respectively. SAPO-34 was the only catalyst that did not form diethyl ether in significant amounts. As temperature increased, the yield to unbranched paraffins increased over SAPO-34. In addition, the yield to propylene and butenes also increased with temperature. Over HZSM-5, yield to unbranched olefins decreased as temperature was increased, while the yield to diethyl ether and paraffin products increased. By inspection of Figure 5b and 5c, the most drastic yield increases over HZSM-5 were observed in propane, butane and isobutane. Despite significant decreases in ethylene yield, the yield to propylene increased with temperature.

The product yields from both mixed alcohol feeds at 300 °C are shown in Figure 4. The total product yield (i.e., total alcohol conversion) increased over Zr-KIT-6 (47% to 58%) and Al-MCM-41 (60% to 83%) when water and higher alcohol concentrations were increased, as shown in Figure 4c-d. Ethanol conversion increased over Al-MCM-41 and decreased over Zr-KIT-6 (Figure 3b and 3d). Conversions of 1-butanol and 1-propanol were >99% in all cases. Total product yield remained near 100% over the zeolite materials in the C_{3+}-alcohol rich feed experiments. Over SAPO-34, there was a slight increase in the yield to paraffins (i.e., propane) when water and higher alcohol concentrations were increased (Figure 4). As will be discussed further in Section 3.3.4, the product distribution over SAPO-34 appeared to be directly related to the composition of the mixed alcohol feed stream. For HZSM-5, product yield to unbranched olefins and diethyl ether decreased while yield to unbranched and branched paraffins increased (Figure 4a and 4c). The decrease in the yield to unbranched olefins was attributed primarily to the decreased yield to ethylene, while the increase in yield to paraffins was ascribed to the increased yield to propane, butane, and isobutane. However; in general, the product distribution of HZSM-5 was not as sensitive to the composition of the mixed alcohol feed as SAPO-34.

3.3.3. Mixed Alcohol Dehydration: Discussion. The observed shift in product selectivity with ethanol conversion over Al-MCM-41 and Zr-KIT-6 agrees with literature reports suggesting that diethyl ether is an intermediate product in ethanol dehydration to ethylene [23]. The greater carbon yield over Al-MCM-41 was an interesting result considering that it contains less than 35% of the total acid sites of Zr-KIT-6, as determined by NH_3-TPD (Table 3). The NH_3-TPD profiles suggested that Al-MCM-41 possessed a greater concentration of strong acid sites than Zr-KIT-6 as evidenced by the desorption peaks at temperatures above 400 °C (Figure S3). The position of the Lewis-bound pyridine adsorption band in the py-DRIFTS spectra (Figure S4) is also an indicator of acid site strength [42,43]. The Al-MCM-41 Lewis peak is located at a higher wavenumber (1455 cm^{-1}) than the Zr-KIT-6 Lewis peak (1445 cm^{-1}), indicative of a qualitatively stronger Lewis acidic site. Thus, Al-MCM-41 had higher strength Lewis acidic sites than Zr-KIT-6. This difference in acidic site strength may be responsible for the observed activity. The higher TOF of Al-MCM-41 also validates the higher total carbon yield and alcohol conversion observed in 300 °C mixed alcohol dehydration experiments compared to Zr-KIT-6 (Figures 3 and 4). Previous work from

Haishi et al. [23] with Al-MCM-41 (Si/Al = 237 mol/mol) materials in ethanol dehydration experiments has shown high yield to ethylene, and observed diethyl ether formation at moderate ethanol conversions. The data presented here corroborates these literature results. The higher total product yields over the mesoporous materials in C_{3+}-alcohol rich feed experiments agree with previously reported results on the dehydration reactivity order of alcohols over Al-MCM-41 (Figure 4). Haishi et al. [23] found that higher alcohols (2-propanol, 1-butanol, 1-propanol) were more easily dehydrated at lower temperature over Al-MCM-41. The order of reactivity of the higher alcohols was consistent with the stability of the carbocations, which led the authors to suggest a reaction mechanism proceeding through a carbocation intermediate as opposed to the diethyl ether intermediate proposed for dehydration of ethanol to ethylene in the same work [23].

The product distribution observed over HZSM-5, including a high yield to butane, isobutane and C_{5+} hydrocarbons, may suggest a mixed alcohol dehydration mechanism similar to the mechanism for methanol/DME-to-hydrocarbons over zeolites (Figure S6) [44-46]. Zeolite catalysts have been shown to be effective for methanol/dimethyl ether conversion to a variety of hydrocarbons, including olefins, aromatics, and branched alkanes [45-48]. The product distribution in these processes is dependent on operating conditions and zeolite type [45]. A methanol/DME-to-hydrocarbons type mechanism involving coupled aromatic and olefin production cycles may explain the invariance of product selectivity with feed composition in mixed alcohol dehydrations over HZSM-5, in which product desorption from the catalyst surface is independent of feed species and occurs before further methylation to higher carbon products [44]. Thus, increasing the concentration of higher alcohols would not be expected to increase yield to higher hydrocarbons.

Based on ethanol conversion (Figure 3a), the zeolite catalysts were active at lower temperatures compared to mesoporous materials. The mixed alcohol dehydration data were supported by the TOF data, where the Brønsted acidic zeolites were shown to be more active for ethanol dehydration than the Lewis acidic silica-based materials (Table 4). As mentioned previously, Zr-KIT-6 and HZSM-5 possess similar acid site densities, but differ in the acid site strength and type (B/L = 0.11 and 13.25, respectively; Table 3). The TOF data imply that Brønsted acidic sites are more active for ethanol dehydration than Lewis acidic sites. Considering the dramatically higher dehydration activity of HZSM-5 compared to Zr-KIT-6, this conclusion can be extended to mixed alcohol dehydration. The ethanol TOF values also suggest that HZSM-5 is more active for ethanol dehydration than SAPO-34. There is evidence that the Brønsted acidic sites of HZSM-5 are stronger than those of SAPO-34 [49]. This difference in acidic site strength likely contributed to the observed difference in the ethanol dehydration TOF between HZSM-5 and SAPO-34. This result is corroborated by Zhang et al. [17], in which HZSM-5 was found to be more active for ethanol dehydration than SAPO-34. Diethyl ether was observed in the intrinsic ethanol dehydration study, but not in the mixed alcohol dehydration studies over SAPO-34. There is literature evidence of intermolecular alcohol dehydration to form the corresponding ether dimer over both Brønsted and Lewis acidic sites [50-52]; however, the exact mechanism for diethyl ether formation and its role in overall ethanol dehydration mechanism over SAPO-34 remains unclear.

SAPO-34 produced unbranched olefins with high yield at all temperatures in ethanol rich feed experiments; however, the yield to paraffins and C_{3+} olefins increased slightly as reaction temperature increased (Figure 4a-b and Figure 5a-d). Temperature also affects olefin selectivity over SAPO-34 in the MTO process, although higher ethylene selectivity is achieved at higher temperatures [53]. The carbon yield over HZSM-5 had a much stronger dependence on reaction temperature in the ethanol rich feed experiments than SAPO-34, despite similar ethanol conversions at all temperatures. At 250 °C, HZSM-5 displayed >85% yield to olefin products (Figure 5a) yet less than 30% yield at 350 °C (Figure 5a and 5c). At all temperatures, SAPO-34 dehydrated the ethanol rich feed stream with higher yield to olefin products than HZSM-5. With naphtha and distillate-range hydrocarbons as a desired final product, C_2-C_4 olefins are the most desirable products from a mixed alcohol feed because of the potential to oligomerize. Thus, while HZSM-5 exhibited the highest yield to higher carbon number products (Figure 4b), the low yield to olefins was undesirable.

Previous research has demonstrated that both HZSM-5 and SAPO-34 are capable of dehydrating ethanol to ethylene with greater than 90% selectivity; however HZSM-5 was shown to be more selective at lower

temperature than SAPO-34 [17]. Despite high ethanol conversions over HZSM-5 in every experiment (>98%, Figure 3), changes in WHSV and temperature did result in changes to the observed product yields (Figure S7). Olefin production over HZSM-5 was favored at lower temperatures and higher WHSV. The total olefin yield over SAPO-34 was independent of WHSV. As mentioned earlier, the product yield over HZSM-5 may be described by a mechanism similar to that of methanol/DME to hydrocarbons. Previous reports suggest the selectivity to light olefins in the methanol-to-hydrocarbons process using HZSM-5 is optimized at low conversion/high WHSV [54]. The data presented here further suggest that light olefin yield over HZSM-5 is maximized at higher WHSVs.

3.3.4. Comparison to MTO. The methanol-to-olefins process has been demonstrated at the semi-commercial scale [10] and uses SAPO-34 as the primary catalyst [12,15,55,56]. The MTO technology was developed to produce ethylene and propylene with high yield and tunable ratios [10]. Yields to ethylene and propylene approaching 90% have been achieved in the UOP/Norsk Hydro process [57], with process temperatures ranging from 450-525 °C and pressures ranging from 34-345 kPa [11]. Bench-scale processes using modified SAPO-34 catalysts have achieved olefin yields near 95% at 450 °C [13]. In comparison, we observed olefin yields of 95% using mixed alcohols at 300 °C (Figure 4c). In the MTO process, the ethylene-to-propylene ratio is adjusted by process operating conditions, but is bounded between 0.5 and 1.5 [55,57]. In the C_{3+}-alcohol rich feed experiments the molar ratio of ethanol to propanol was 2.38 and the molar ratio of ethylene to propylene after dehydration over SAPO-34 was between 2.32 and 2.82 depending on WHSV (Table 5). In addition to achieving comparable olefin yields at lower temperature, mixed alcohol dehydration over SAPO-34 may also offer the ability to produce olefins in a much wider range of ratios based on the composition of the feed stream, which is dictated by the separation and recycle strategies coupled with the mixed alcohol synthesis process. For example, mixed alcohol feeds may have ethanol to propanol molar ratios near 3.25 under the assumptions made for the C_{3+}-alcohol rich feed stream regarding moderate post-synthesis product stream refining [7]. Table 5 suggests that the ethylene to propylene product ratio is strongly dependent on the alcohol feed mixture, reaction temperature, and to a lesser degree the WHSV. As such, reaction temperature and refining the synthesized mixed alcohol feed stream to tune its composition may enable control of the olefin distribution following dehydration. The strong dependence of the ethylene to propylene ratio on the ethanol to propanol feed ratio over SAPO-34 suggests alcohols were directly dehydrated to olefins, and that the hydrocarbon pool chemistry of the MTO process [45,58] did not play a major role.

Table 5. Ethylene to propylene ratio in mixed alcohol dehydration experiments over zeolite catalysts.

Temperature (°C)	**Feed Mixture**	**Ethanol: 1-Propanol in Feed (mol/mol)**	**Catalyst**	**Ethylene:Propylene in Product (mol/mol)**		
				WHSV = 1.3 h^{-1}	**0.64 h^{-1}**	**0.32 h^{-1}**
250 °C	Ethanol Rich	84.1	SAPO-34	42.1	39.6	36.9
			HZSM-5	23.2	16.0	9.30
300 °C	Ethanol Rich	84.1	SAPO-34	27.1	17.3	14.3
			HZSM-5	5.63	3.10	1.54
300 °C	C_{3+}-Alcohol Rich	2.4	SAPO-34	2.82	2.53	2.32
			HZSM-5	2.75	1.70	1.03
350 °C	Ethanol Rich	84.1	SAPO-34	13.8	10.3	7.8
			HZSM-5	1.08	0.757	0.711

3.4. Structural and Chemical Characterization: Post-Reaction

3.4.1. X-Ray Diffraction. Post-reaction SAXS and PXRD patterns are shown in Figures 6 and 7 respectively. A reference diffraction pattern is given for quartz (JCPDS 00-002-0278) in Figure 7a and 7b, and a reference diffraction pattern for graphitic carbon (JCPDS 00-041-1487) is given in Figure 7b as trace amounts of these diluents are likely present in the post-reaction catalyst samples. Reference cards for SiC were omitted for simplicity since reflections associated with SiC phases represented only minor contributions in post-reaction samples. All major features of the PXRD patterns are retained in the post-reaction samples. The PXRD and SAXS data do not suggest any changes to catalyst micro- and meso-structures as a result of exposure to mixed alcohols at temperatures between 250 and 350 °C and up to 10 h TOS.

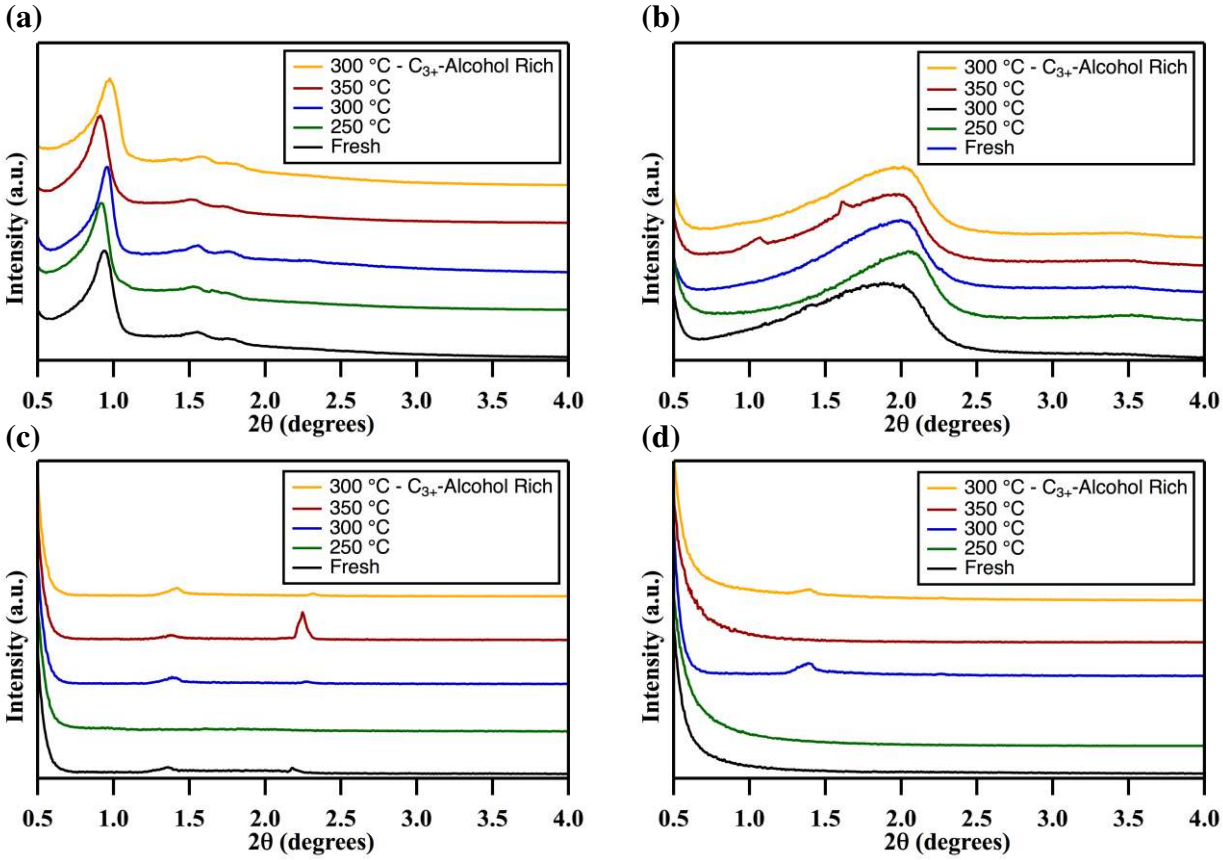

Figure 6. Small angle scattering patterns for post-reaction catalysts. (a) Zr-KIT-6, (b) Al-MCM-41, (c) SAPO-34 and (d) HZSM-5. Fresh catalyst scattering patterns are shown for reference. Peaks at 1.4 ° and 2.3 ° in (c-d), or 1.1 ° and 1.7 ° in (b), are due to the glass tray and are not indicative of mesoporous features.

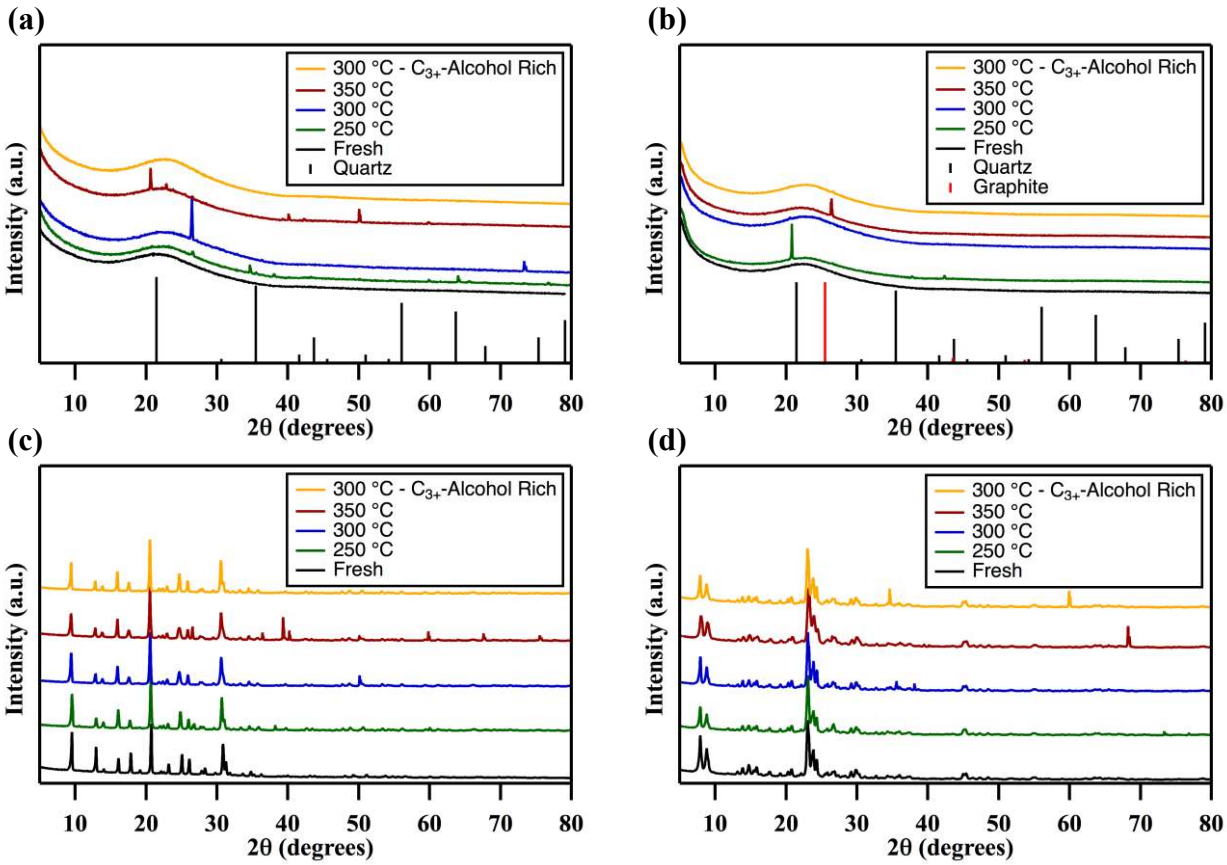

Figure 7. Powder X-Ray Diffractograms for post-reaction catalysts. (a) Zr-KIT-6, (b) Al-MCM-41, (c) SAPO-34 and (d) HZSM-5. Quartz (SiO_2, black lines) and Graphite (C, red lines) reference diffraction patterns are shown for (a) and (c).

3.4.2. Post-Reaction Organic Species. Based on the feed stream flow rates and conservatively assuming each condition was held for 2 h, the maximum amount of carbon remaining on post-reaction samples would be 1.75 g. Solution phase ^{1}H NMR allows for identification and quantification of soluble organic species, including known coke precursors such as hexmethylbenzene (HMB) [59]. Water and components of the alcohol feed (i.e., ethanol, 1-propanol, 1-butanol) were found in most post-reaction ^{1}H NMR spectra. Other organic species were present in negligible amounts (e.g., HMB < 0.007 wt%) on several samples. No other organic species were identified in solution-phase NMR samples.

Solid-state ^{13}C NMR was used as a complementary technique for identifying compounds remaining on the catalyst surface after reaction and those that may not have been detected by solution phase ^{1}H NMR. Table 6 presents ^{13}C solid-state NMR data integrated by functional group and presented as a percentage of total integrated area, as ^{13}C solid-state NMR data is typically only semi-quantitative. Spectra and functional group ^{13}C NMR shift assignments are provided in Figure 8. The alkene functional group chemical shift is typically assigned between 100-150 ppm [60], and may overlap with aromatic compounds. The light olefins produced in the experiments of this work were unlikely to remain on the post-reaction catalyst surface. Thus it is improbable alkenes contributed to the functional group integrations of HZSM-5 and SAPO-34 catalysts. Alcohols, esters and alkanes remaining on the catalyst surface after reaction are likely adsorbed reactants and reaction products; however, aliphatic carbons of alkylated aromatic species are also found in the alkane functional group range and were likely present in the ^{13}C NMR spectra of the post-reaction SAPO-34 samples. Further evidence for the contribution of these aliphatic carbons of alkylated aromatic species is given in the elemental analysis discussion below. By inspection of Figure 8, the signal-

to-noise in the NMR spectra of HZSM-5 samples decreased as the reaction temperature increased. The signal-to-noise for the HZSM-5 is low at higher temperature due to unknown paramagnetic impurities in the samples. Experimental parameters, sample volumes, number of scans (30k), and acquisition times for all data presented in Figure 8 were similar. In an attempt to improve the signal-to-noise, the 300 °C and 350 °C post-reaction samples from the ethanol rich feed were collected for additional scans, 75k and 86k scans respectively. No appreciable increase in signal-to-noise was observed. Higher reaction temperature led to more aromatic compounds relative to the total integrated area of SAPO-34 samples. The aromatic contribution over HZSM-5 was invariant with reaction temperature. Alkyl aromatic species have been shown to control olefin selectivity over SAPO-34 in the MTO process, yet lead to the formation of polycyclic aromatic species and deactivation as a result of pore blockage [61]. Deactivation in mixed alcohol dehydration may be less severe due to lower reaction temperatures (≤300 °C) compared to those generally used in the MTO process (≥400 °C) [55,61].

Table 6. Solid-state ^{13}C NMR results: functional group integrations.

Catalyst	Temperature (°C)	Feed Mixture	Functional Group (%), [chemical shift (ppm)]				
			Ketones & Aldehydes, [190-220]	Carboxyl, [165-190]	Aromatics & Alkenes [100-165]	Alcohols & Esters, [55-95]	Alkanes, [0-55]
Zr-KIT-6	250	Ethanol Rich	-	-	-	62.3	37.7
	300	Ethanol Rich	-	-	-	64.3	35.7
	300	C_{3+}-Alcohol Rich	-	-	-	59.7	40.3
	350	Ethanol Rich	-	-	-	68.8	31.3
Al-MCM-41	250	Ethanol Rich	-	-	-	66.7	33.3
	300	Ethanol Rich	-	-	-	70.6	29.4
	300	C_{3+}-Alcohol Rich	-	-	-	64.4	35.6
	350	Ethanol Rich	-	-	-	74.8	25.2
SAPO-34	250	Ethanol Rich	-	-	28.6	-	71.4
	300	Ethanol Rich	-	-	59.3	-	40.7
	300	C_{3+}-Alcohol Rich	-	1.0	52.8	-	46.3
	350	Ethanol Rich	-	-	87.5	-	12.5
HZSM-5*	250	Ethanol Rich	-	-	32.4	-	67.6
	300	Ethanol Rich	-	-	30.0	-	70.0
	300	C_{3+}-Alcohol Rich	-	-	18.7	-	81.3
	350	Ethanol Rich	-	-	33.9	22.0	44.1

* Signal-to-noise was low

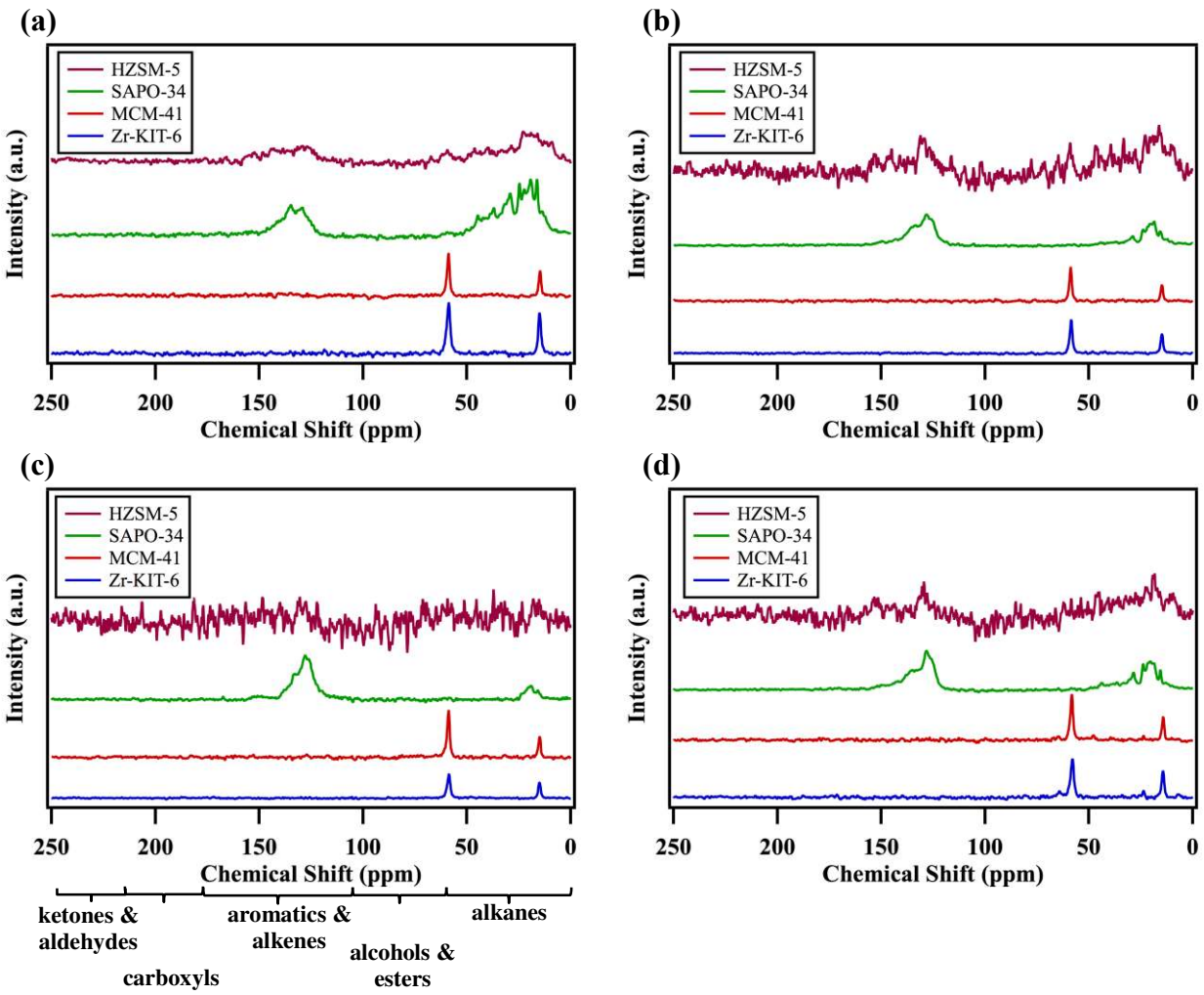

Figure 8. Solid-state NMR spectra for post-reaction catalysts run at (a) 250 °C, (b) 300 °C and (c) 350 °C with the ethanol rich feed stream and (d) with the C_{3+}-alcohol rich feed at 300 °C. Function group regions are show below (c) for reference.

The results from the elemental analysis of the post-reaction catalyst samples are presented in Table 7. The hydrogen to carbon molar ratio (H/C) is presented alongside carbon and hydrogen weight percentage in Table 7. The post-reaction mesoporous materials contained comparable amounts of carbon and hydrogen. Given the NMR results and the high (>3) H/C ratio, it is probable that the carbon and hydrogen present on these post-reaction samples was due to residual alcohols and water. Water likely inflated the hydrogen to carbon molar ratio, resulting in H/C ratios above that of ethanol (H/C = 3). A decrease in the carbon content at 350 °C may be the result of greater alcohol desorption as the reactor was cooled from the higher reaction temperature. The post-reaction SAPO-34 catalyst contained the most carbon at a given reaction temperature, and had lower H/C ratios (<2.4) than the post-reaction mesoporous materials. SAPO-34 also had the smallest pores (Table 2), thus larger carbonaceous compounds that could leave the pores of HZSM-5, Zr-KIT-6 and Al-MCM-41 may not have escaped the pores of SAPO-34. The low H/C ratio, combined with the solid-state NMR data, suggested the carbon was aromatic in nature. HZSM-5 also displayed high carbon content and low H/C ratios in all but the 350 °C sample. In light of the elemental analysis of post-reaction HZSM-5 catalyst samples, the ^{13}C solid-state NMR data seem to indicate the presence of an unknown paramagnetic impurity in the sample that is interfering with the NMR signal intensity as discussed previously. Alcohol functional groups were not detected in solid-state ^{13}C NMR of post-reaction

SAPO-34 samples, thus alcohol desorption is not an explanation for the decrease in carbon content with higher reaction temperature. Given the solid-state NMR data, it is plausible that alkylated aromatics made up a larger percentage of detected compounds at lower reaction temperatures. Alkylated single-ring aromatic compounds are known to form in the pores of SAPO-34 during the MTO reaction [12,61,62] and the solid-state ^{13}C NMR data suggests aliphatic carbons constitute a larger percentage of detected carbon containing compounds on lower reaction temperature samples. Increasing the C_{3+} alcohol and water concentrations in the feed stream did not affect the detected carbon content of the 300 °C SAPO-34 sample, and the solid-state NMR suggests aromatic compounds are still present. This was in contrast to the HZSM-5 samples from 300 °C experiments in which the carbon content was drastically lower and the functional group distribution of the solid-state NMR spectra shifted to favor alkanes; the underlying cause remains unclear. The elemental analysis data corroborates the ^{1}H and ^{13}C NMR data and confirms SAPO-34 was the most prone to aromatic carbon accumulation at all temperatures. Understanding the role of these aromatic compounds in the catalytic reaction mechanism and long term stability will be the focus of future work.

Table 7. Elemental analysis of post-reaction catalysts.

Catalyst	Temperature (°C)	Feed Mixture	C (wt%)	H (wt%)	H/C molar ratio
Zr-KIT-6	250	Ethanol Rich	2.9	1.3	5.3
	300	Ethanol Rich	2.9	0.97	4.0
	300	C_{3+}-Alcohol Rich	3.0	1.2	4.7
	350	Ethanol Rich	1.9	0.73	4.6
Al-MCM-41	250	Ethanol Rich	1.7	0.72	4.9
	300	Ethanol Rich	2.9	0.77	3.1
	300	C_{3+}-Alcohol Rich	2.3	0.75	3.8
	350	Ethanol Rich	2.2	0.65	3.6
SAPO-34	250	Ethanol Rich	9.9	2.0	2.4
	300	Ethanol Rich	10.5	2.0	2.3
	300	C_{3+}-Alcohol Rich	10.3	1.7	2.0
	350	Ethanol Rich	6.1	1.1	2.2
HZSM-5	250	Ethanol Rich	5.5	0.97	2.1
	300	Ethanol Rich	6.5	0.56	1.0
	300	C_{3+}-Alcohol Rich	3.4	0.56	2.0
	350	Ethanol Rich	1.9	0.73	4.5

3.5. Acid Site Characterization: Post-Reaction

All post-reaction catalysts exhibited a decrease in total acid sites determined by NH_3-TPD, even after regeneration in air (Table 8). The decreases in detectable acid sites appeared to be dependent on reaction temperature, where significant decreases in total acid sites were observed when the reaction temperature was increased from 300 to 350 °C. Below 350 °C, the mesoporous materials displayed more dramatic acid site loss than the zeolite catalysts. At reaction temperatures of 300 °C or lower, the percent acid site loss of the zeolite catalysts ranged from 3.6 to 11.0%, whereas over Al-MCM-41 and Zr-KIT-6, the range was 18.5 to 36.0%. There were also interesting trends in the py-DRIFTS data of post-reaction samples without an air regeneration step. With the exception of the C_{3+}-alcohol feed experiment, the B/L ratios of the post-reaction Al-MCM-41 samples were higher than the fresh catalyst sample, indicating selective loss of detectable Lewis acidic sites; however, the underlying cause remains unclear. With the exception of the C_{3+}-alcohol rich feed experiment, the B/L ratio of HZSM-5 decreased as reaction temperature increased. It

is important to note that a decrease in B/L ratios determined by py-DRIFTS (and corresponding total acid sites determined by NH_3-TPD) depend on surface accessibility of the pyridine (or NH_3) probe molecule. For example, carbonaceous deposits on the catalyst surface may (i) block sites from pyridine that are still functionally active under reaction conditions, (ii) alter the surface hydrophilicity resulting in lower pyridine adsorption, and (iii) increase the catalyst material weight leading to lower mass-normalized values. These effects are likely decreased in the NH_3-TPD data due to the regeneration step, yet must not be dismissed. Nevertheless, significant changes to the acid site content and B/L ratio are evident after reaction. The mesoporous materials appeared to be more sensitive to acid site loss, and changes to the B/L ratio are evident on both types of materials.

Table 8. Acid site characterization for post-reaction catalysts.

Catalyst	Temperature, °C	Feed Mixture	B/L ratio	Total Acid Sites (µmol/g)	Loss of Total Acid Sites (%)
Zr-KIT-6	Fresh	-	0.11	785	-
	250	Ethanol Rich	All Lewis	601	23.4
	300	Ethanol Rich	All Lewis	640	18.5
	300	C_{3+}-Alcohol Rich	0.62	590	24.8
	350	Ethanol Rich	0.10	275	65.0
Al-MCM-41	Fresh	-	0.03	264	-
	250	Ethanol Rich	0.77	188	28.8
	300	Ethanol Rich	0.33	193	26.9
	300	C_{3+}-Alcohol Rich	All Lewis	169	36.0
	350	Ethanol Rich	0.50	207	21.6
SAPO-34	Fresh	-	n/a	1700	-
	250	Ethanol Rich	n/a	1620	4.7
	300	Ethanol Rich	n/a	1620	4.8
	300	C_{3+}-Alcohol Rich	n/a	1640	3.6
	350	Ethanol Rich	n/a	863	49.2
HZSM-5	Fresh	-	13.25	998	-
	250	Ethanol Rich	10.67	890	10.8
	300	Ethanol Rich	8.73	908	9.0
	300	C_{3+}-Alcohol Rich	All Brønsted	889	11.0
	350	Ethanol Rich	6.18	451	54.8

* Total acid sites of post-reaction samples was determined after regeneration in air at 500 °C.

4. Conclusions

The Brønsted acidic zeolite materials, HZSM-5 and SAPO-34, displayed high activity for mixed alcohol dehydration with >98 % ethanol conversion observed in all experiments. The Lewis acidic mesoporous materials were less active and produced non-negligible amounts of diethyl ether, limiting their yield to desired olefins. Olefin yields over SAPO-34 were comparable to those found in the MTO process, yet were achieved at lower temperature. In addition, the olefin product distribution over SAPO-34 was directly related to the composition of the mixed alcohol feed, and thus may offer more flexibility than the MTO process in controlling the olefin distribution; however, as temperature was increased, side reactions began to negatively impact olefin yields. Side reactions were more problematic over HZSM-5, even at low reaction temperatures. Catalyst lifetime was not explored within this manuscript and needs to be evaluated

in future work. Solid-state ^{13}C NMR and elemental analysis studies indicated that SAPO-34 was more prone to aromatic carbon deposition than its zeolite counterpart HZSM-5, while no aromatic carbon was found on post-reaction Zr-KIT-6 and Al-MCM-41 catalysts. The role of these aromatic compounds on long-term stability in mixed alcohol dehydration reactions, and the regeneration potential of SAPO-34 remain important considerations for future research.

The research presented here, demonstrating the successful dehydration of a mixed alcohol feed to corresponding olefin products, provides a foundation for future developments in hydrocarbon production from biomass-derived syngas through mixed alcohol intermediates. The characterization and ethanol dehydration experiments provide evidence of carbon deposition, changes to acidic sites, regeneration potential, and intrinsic dehydration activity of Brønsted and Lewis acidic materials. Thus these experiments supplement the mixed alcohol dehydration studies to provide valuable insights into the underlying principles and potential applicability of mixed alcohol dehydration in the indirect liquefaction pathway. In this regard, mixed alcohol dehydration may provide unique advantages, such as tunable olefin composition and lower operating temperature.

Acknowledgements: This work was supported by the Department of Energy Bioenergy Technologies Office under Contract no. DE-AC36-080GO28308. The authors would also like to thank Dr. Matthew Yung for assistance with X-ray diffraction experiments and Carrie Farberow for help in creating the graphical abstract.

References

[1] L.P. Koh, J. Ghazoul, Biofuels, biodiversity, and people: Understanding the conflicts and finding opportunities, Biol. Conserv., 141 (2008) 2450-2460.
[2] A.J. Ragauskas, C.K. Williams, B.H. Davison, G. Britovsek, J. Cairney, C.A. Eckert, W.J. Frederick, J.P. Hallett, D.J. Leak, C.L. Liotta, J.R. Mielenz, R. Murphy, R. Templer, T. Tschaplinski, The path forward for biofuels and biomaterials, Science, 311 (2006) 484-489.
[3] T.R. Brown, A techno-economic review of thermochemical cellulosic biofuel pathways, Bioresource Technology, 178 (2015) 166-176.
[4] A.B. Lovins, Winning the oil endgame : innovation for profits, jobs and security, 1st ed., Rocky Mountain Institute, Snowmass, Colo., 2004.
[5] R. Schnepf, B.D. Yacobucci, Renewable Fuel Standard (RFS): Overview and Issues (R40155; March 14, 2013), U.S. Congressional Research Service.
[6] G.W. Huber, J.A. Dumesic, An overview of aqueous-phase catalytic processes for production of hydrogen and alkanes in a biorefinery, Catal Today, 111 (2006) 119-132.
[7] J.E. Hensley, T.M. Lovestead, E. Christensen, A. Dutta, T.J. Bruno, R. McCormick, Compositional Analysis and Advanced Distillation Curve for Mixed Alcohols Produced via Syngas on a K-CoMoSx Catalyst, Energ Fuel, 27 (2013) 3246-3260.
[8] E.C.D. Tan, M. Talmadge, A. Dutta, J.E. Hensley, J.A. Schaidle, M. Biddy, D. Humbird, L.J. Snowden-Swan, R. Yap, J. Lukas, Process Design and Economics for the Conversion of Lignocellulosic Biomass to Hydrocarbons via Indirect Liquefaction (NREL/TP-5100-62402; March 2015), U.S. Department of Energy Bioenergy Technologies Office.
[9] G.W. Huber, S. Iborra, A. Corma, Synthesis of transportation fuels from biomass: chemistry, catalysts, and engineering, Chemical reviews, 106 (2006) 4044-4098.
[10] J.Q. Chen, A. Bozzano, B. Glover, T. Fuglerud, S. Kvisle, Recent advancements in ethylene and propylene production using the UOP/Hydro MTO process, Catal Today, 106 (2005) 103-107.
[11] P.T. Barger, S.T. Wilson, J.S. Holmgren, Metal aluminophosphate catalyst for converting methanol to light olefins, UOP, United States, 1992.
[12] D. Chen, K. Moljord, T. Fuglerud, A. Holmen, The effect of crystal size of SAPO-34 on the selectivity and deactivation of the MTO reaction, Microporous Mesoporous Mat., 29 (1999) 191-203.
[13] P. Wang, D. Yang, J. Hu, J.a. Xu, G. Lu, Synthesis of SAPO-34 with small and tunable crystallite size by two-step hydrothermal crystallization and its catalytic performance for MTO reaction, Catal Today, 212 (2013) 62.e61-62.e68.
[14] J. Jong Won, J. Jaewoo, K. Chul-Ung, J. Kwang-Eun, J. Soon-Yong, J. Sung Hwa, Synthesis of Mesoporous SAPO-34 Molecular Sieves and Their Applications in Dehydration of Butanols and Ethanol, Journal of Nanoscience and Nanotechnology, 13 (2013) 2782-2788.
[15] Y. Chen, Y.L. Wu, L. Tao, B. Dai, M.D. Yang, Z. Chen, X.Y. Zhu, Dehydration reaction of bio-ethanol to ethylene over modified SAPO catalysts, J. Ind. Eng. Chem., 16 (2010) 717-722.
[16] I. Takahara, M. Saito, M. Inaba, K. Murata, Dehydration of ethanol into ethylene over solid acid catalysts, Catal. Lett., 105 (2005) 249-252.
[17] X. Zhang, R.J. Wang, X.X. Yang, F.B. Zhang, Comparison of four catalysts in the catalytic dehydration of ethanol to ethylene, Microporous Mesoporous Mat., 116 (2008) 210-215.
[18] M. Zhang, Y. Yu, Dehydration of Ethanol to Ethylene, Ind Eng Chem Res, 52 (2013) 9505-9514.
[19] J. Ouyang, F.X. Kong, G.D. Su, Y.C. Hu, Q.L. Song, Catalytic Conversion of Bio-ethanol to Ethylene over La-Modified HZSM-5 Catalysts in a Bioreactor, Catal. Lett., 132 (2009) 64-74.
[20] R.V. Ermakov, V.A. Plakhotnik, Conversion of lower alcohols into C-2-C-4 olefins over acid-base catalysts, Petrol Chem+, 48 (2008) 1-5.
[21] K.K. Ramasamy, Y. Wang, Catalyst activity comparison of alcohols over zeolites, J. Energy Chem., 22 (2013) 65-71.
[22] M. Iwamoto, K. Kasai, T. Haishi, Conversion of Ethanol into Polyolefin Building Blocks: Reaction Pathways on Nickel Ion-loaded Mesoporous Silica, Chemsuschem, 4 (2011) 1055-1058.
[23] T. Haishi, K. Kasai, M. Iwamoto, Fast and Quantitative Dehydration of Lower Alcohols to Corresponding Olefins on Mesoporous Silica Catalyst, Chem. Lett., 40 (2011) 614-616.
[24] Q. Pan, A. Ramanathan, W.K. Snavely, R.V. Chaudhari, B. Subramaniam, Intrinsic Kinetics of Ethanol Dehydration Over Lewis Acidic Ordered Mesoporous Silicate, Zr-KIT-6, Top. Catal., 57 (2014) 1407-1411.

[25] Q. Pan, A. Ramanathan, W.K. Snavely, R.V. Chaudhari, B. Subramaniam, Synthesis and Dehydration Activity of Novel Lewis Acidic Ordered Mesoporous Silicate: Zr-KIT-6, Ind Eng Chem Res, 52 (2013) 15481-15487.
[26] Y. Gucbilmez, T. Dogu, S. Balci, Ethylene and acetaldehyde production by selective oxidation of ethanol using mesoporous V-MCM-41 catalysts, Ind Eng Chem Res, 45 (2006) 3496-3502.
[27] A.T. Aguayo, A.G. Gayubo, A.M. Tarrio, A. Atutxa, J. Bilbao, Study of operating variables in the transformation of aqueous ethanol into hydrocarbons on an HZSM-5 zeolite, J. Chem. Technol. Biotechnol., 77 (2002) 211-216.
[28] I. Takahara, M. Saito, H. Matsuhashi, M. Inaba, K. Murata, Increase in the number of acid sites of a H-ZSM5 zeolite during the dehydration of ethanol, Catal. Lett., 113 (2007) 82-85.
[29] D. Arias, A. Colmenares, M.L. Cubeiro, J. Goldwasser, C.M. Lopez, F.J. Machado, V. Sazo, The transformation of ethanol over AlPO4 and SAPO molecular sieves with AEL and AFI topology. Kinetic and thermodynamic approach, Catal. Lett., 45 (1997) 51-58.
[30] H. Oikawa, Y. Shibata, K. Inazu, Y. Iwase, K. Murai, S. Hyodo, G. Kobayashi, T. Baba, Highly selective conversion of ethene to propene over SAPO-34 as a solid acid catalyst, Appl Catal a-Gen, 312 (2006) 181-185.
[31] J.M. Müller, G.C. Mesquita, S.M. Franco, L.D. Borges, J.L. de Macedo, J.A. Dias, S.C.L. Dias, Solid-state dealumination of zeolites for use as catalysts in alcohol dehydration, Microporous Mesoporous Mat., 204 (2015) 50-57.
[32] C.B. L.B. McCusker, Database of Zeolite Structures.
[33] M. Sawa, M. Niwa, Y. Murakami, Relationship between acid amount and framework aluminum content in mordenite, Zeolites, 10 (1990) 532-538.
[34] N. Katada, H. Igi, J.-H. Kim, Determination of the Acidic Properties of Zeolite by Theoretical Analysis of Temperature-Programmed Desorption of Ammonia Based on Adsorption Equilibrium, The Journal of Physical Chemistry B, 101 (1997) 5969-5977.
[35] S.M. Maier, A. Jentys, J.A. Lercher, Steaming of Zeolite BEA and Its Effect on Acidity: A Comparative NMR and IR Spectroscopic Study, The Journal of Physical Chemistry C, 115 (2011) 8005-8013.
[36] C.A. Emeis, Determination of Integrated Molar Extinction Coefficients for Infrared Absorption Bands of Pyridine Adsorbed on Solid Acid Catalysts, J Catal, 141 (1993) 347-354.
[37] A. Ramanathan, B. Subramaniam, R. Maheswari, U. Hanefeld, Synthesis and characterization of Zirconium incorporated ultra large pore mesoporous silicate, Zr-KIT-6, Microporous Mesoporous Mat., 167 (2013) 207-212.
[38] C.T. Kresge, M.E. Leonowicz, W.J. Roth, J.C. Vartuli, J.S. Beck, Ordered mesoporous molecular sieves synthesized by a liquid-crystal template mechanism, Nature, 359 (1992) 710-712.
[39] J. Jae, G.A. Tompsett, A.J. Foster, K.D. Hammond, S.M. Auerbach, R.F. Lobo, G.W. Huber, Investigation into the shape selectivity of zeolite catalysts for biomass conversion, J Catal, 279 (2011) 257-268.
[40] S. Ashtekar, S.V.V. Chilukuri, D.K. Chakrabarty, SMALL-PORE MOLECULAR-SIEVES SAPO-34 AND SAPO-44 WITH CHABAZITE STRUCTURE - A STUDY OF SILICON INCORPORATION, J. Phys. Chem., 98 (1994) 4878-4883.
[41] F. Lonyi, J. Valyon, On the interpretation of the NH3-TPD patterns of H-ZSM-5 and H-mordenite, Microporous Mesoporous Mat., 47 (2001) 293-301.
[42] E.A. Paukshtis, E.N. Yurchenko, USE OF IR-SPECTROSCOPY IN STUDIES OF ACID-BASIC PROPERTIES OF HETEROGENEOUS CATALYSTS, Uspekhi Khimii, 52 (1983) 426-454.
[43] M.I. Zaki, M.A. Hasan, L. Pasupulety, Surface reactions of acetone on Al2O3, TiO2, ZrO2, and CeO2: IR spectroscopic assessment of impacts of the surface acid-base properties, Langmuir, 17 (2001) 768-774.
[44] D.A. Simonetti, R.T. Carr, E. Iglesia, Acid strength and solvation effects on methylation, hydride transfer, and isomerization rates during catalytic homologation of C-1 species, J Catal, 285 (2012) 19-30.
[45] S. Ilias, A. Bhan, Mechanism of the Catalytic Conversion of Methanol to Hydrocarbons, ACS Catal., 3 (2013) 18-31.
[46] S. Ilias, A. Bhan, Tuning the selectivity of methanol-to-hydrocarbons conversion on H-ZSM-5 by co-processing olefin or aromatic compounds, J Catal, 290 (2012) 186-192.
[47] J.F. Haw, W.G. Song, D.M. Marcus, J.B. Nicholas, The mechanism of methanol to hydrocarbon catalysis, Accounts Chem. Res., 36 (2003) 317-326.

[48] J.H. Ahn, B. Temel, E. Iglesia, Selective Homologation Routes to 2,2,3-Trimethylbutane on Solid Acids, Angew. Chem.-Int. Edit., 48 (2009) 3814-3816.
[49] J.F. Haw, Zeolite acid strength and reaction mechanisms in catalysis, Physical Chemistry Chemical Physics, 4 (2002) 5431-5441.
[50] B.C. Shi, B.H. Davis, Alcohol dehydration: Mechanism of ether formation using an alumina catalyst, J Catal, 157 (1995) 359-367.
[51] J.N. Kondo, K. Ito, E. Yoda, F. Wakabayashi, K. Domen, An ethoxy intermediate in ethanol dehydration on bronsted acid sites in zeolite, J. Phys. Chem. B, 109 (2005) 10969-10972.
[52] C.P. Bezoukhanova, Y.A. Kalvachev, ALCOHOL REACTIVITY ON ZEOLITES AND MOLECULAR-SIEVES, Catal. Rev.-Sci. Eng., 36 (1994) 125-143.
[53] S. Wilson, P. Barger, The characteristics of SAPO-34 which influence the conversion of methanol to light olefins, Microporous Mesoporous Mat., 29 (1999) 117-126.
[54] C.D. Chang, METHANOL CONVERSION TO LIGHT OLEFINS, Catal. Rev.-Sci. Eng., 26 (1984) 323-345.
[55] T. Mokrani, M. Scurrell, Gas Conversion to Liquid Fuels and Chemicals: The Methanol Route-Catalysis and Processes Development, Catal. Rev.-Sci. Eng., 51 (2009) 1-145.
[56] I.M. Dahl, R. Wendelbo, A. Andersen, D. Akporiaye, H. Mostad, T. Fuglerud, The effect of crystallite size on the activity and selectivity of the reaction of ethanol and 2-propanol over SAPO-34, Microporous Mesoporous Mat., 29 (1999) 159-171.
[57] P.T. Barger, B.V. Vora, P.R. Pujado, Q.J. Chen, Converting natural gas to ethylene and propylene using the UOP/HYDRO MTO process, in: M. Anpo, M. Onaka, H. Yamashita (Eds.) Science and Technology in Catalysis 2002, Kodansha Ltd, Tokyo, 2003, pp. 109-114.
[58] C.M. Wang, Y.D. Wang, Z.K. Xie, Insights into the reaction mechanism of methanol-to-olefins conversion in HSAPO-34 from first principles: Are olefins themselves the dominating hydrocarbon pool species?, J Catal, 301 (2013) 8-19.
[59] M. Bjorgen, U. Olsbye, S. Kolboe, Coke precursor formation and zeolite deactivation: mechanistic insights from hexamethylbenzene conversion, J Catal, 215 (2003) 30-44.
[60] E.J. Munson, A.A. Kheir, N.D. Lazo, J.F. Haw, INSITU SOLID-STATE NMR-STUDY OF METHANOL-TO-GASOLINE CHEMISTRY IN ZEOLITE HZSM-5, J. Phys. Chem., 96 (1992) 7740-7746.
[61] W.L. Dai, G.J. Wu, L.D. Li, N.J. Guan, M. Hunger, Mechanisms of the Deactivation of SAPO-34 Materials with Different Crystal Sizes Applied as MTO Catalysts, ACS Catal., 3 (2013) 588-596.
[62] D. Chen, H.P. Rebo, K. Moljord, A. Holmen, Influence of coke deposition on selectivity in zeolite catalysis, Ind Eng Chem Res, 36 (1997) 3473-3479.